THE EUROPEAN
PHYSICAL JOURNAL A

# Determination of thermal neutron capture cross-section of cerium isotopes

**Samrudhi R. Kanjarpane**[1,a], **P. M. Prajapati**[1,2,3,b], **Sachin Shet**[4,c], **Bhargav Soni**[5,d], **Deep Bhandari**[6,e], **Rajeev Kumar**[6,7,f], **R. G. Pizzone**[8,2,g], **S. V. Suryanarayana**[9,h]

[1] Manipal Center for Natural Sciences, Manipal Academy of Higher Education, Manipal 576104, India
[2] Istituto Nazionale di Fisica Nucleare, Laboratori Nazionali del Sud, 95123 Catania, Italy
[3] Applied Physics Department, School of Science, ITM SLS Baroda University, Vadodara 391510, India
[4] Department of Physics, Manipal Institute of Technology, Manipal Academy of Higher Education, Manipal 576104, India
[5] Physics Department, Faculty of Science, The Maharaja Sayajirao University of Baroda, Vadodara 390002, India
[6] Reactor Physics Design Division, Bhabha Atomic Research Centre, Mumbai 400085, India
[7] Homi Bhabha National Institute, Bhabha Atomic Research Centre, Mumbai 400094, India
[8] Dipartimento di Fisica e Astronomia, Ettore Majorana, Universitá di Catania, Catania 95123, Italy
[9] Nuclear Physics Division, Bhabha Atomic Research Centre, Mumbai 400085, India

Communicated by Aurora Tumino

**Abstract** The thermal neutron capture cross-section of cerium isotopes $^{140}$Ce and $^{142}$Ce, were measured with detailed covariance analysis using naturally occurring cerium oxide samples. We conducted irradiation with an Am–Be neutron source at the Manipal Institute of Technology and performed offline gamma-ray measurements via High Purity Germanium (HPGe) Detector. The neutron spectrum from the irradiation location was obtained by employing multiple foil activation techniques and spectrum unfolding methods. The present results provide precise thermal neutron capture cross-section data with detailed covariance analysis. The measured cross sections,  $0.54 \pm 0.03$ barns for $^{140}$Ce and $0.83 \pm 0.04$ barns for cerium-142, are compared with previous measurements and with the latest available evaluated nuclear libraries. It is observed that the presently measured thermal cross-section values of $^{140}$Ce and $^{142}$Ce are lower than the evaluated data but have higher accuracy compared to the previous measurements with larger uncertainties. Further, the measured thermal neutron capture cross-section values of $^{140}$Ce and $^{142}$Ce isotopes are in good agreement with the previous measurements than the evaluations. Thus, the current state of nuclear data evaluation requires improvement for cerium isotopes.

## 1 Introduction

The low-energy neutron cross-section data of cerium isotopes are crucial for various scientific and industrial applications. Cerium (Ce), with its most abundant isotopes being $^{136,138,140,142}$Ce [1], plays a pivotal role in nuclear technology and science. Cerium isotopes particularly, $^{140}$Ce and $^{142}$Ce are present in nuclear fuels and fission products. Accurate neutron cross-section data of cerium helps in reactor core design, fuel cycle analysis, and criticality safety assessments. It aids in predicting long-term radiological hazards and optimizing waste disposal strategies. Further, experimental neutron cross-section measurements of cerium isotopes help validate and improve nuclear data libraries [2–4]. This enhances the accuracy of neutron transport codes used in reactor physics and nuclear security. In context of astrophysics [5], cerium isotopes play an important role in s-process nucleosynthesis [6,7]. Neutron capture cross-section data of cerium isotopes provide insight into element formation in stars. In general, precise low-energy neutron cross-section data of cerium isotopes are essential for both fundamental nuclear science and practical applications in reactor technology, waste management, and astrophysics.

The cross-section data from previous measurements obtained from the EXFOR database [9] provide a compre-

[a] e-mail: samrudhirkanjarpane@gmail.com

[b] e-mail: paresh.physics@itmbu.ac.in (corresponding author)

[c] e-mail: shet.sachin@manipal.edu

[d] e-mail: sonibhargav15@gmail.com

[e] e-mail: dbhan@barc.gov.in

[f] e-mail: rajeevk@barc.gov.in

[g] e-mail: rgpizzone@lns.infn.it

[h] e-mail: suryanarayan7@yahoo.com

**Table 1** Details of Different isotopes of Cerium [8]

| Capture by | Product | Abundance(%) | Half life | Gamma rays (keV) |
| --- | --- | --- | --- | --- |
| Ce-136 | Ce-137 | 0.18 | 34.4 h | 254.2 (11.0%) |
| Ce-138 | Ce-139 | 0.25 | 137.64 d | 165.9 (79.9%) |
| Ce-140 | Ce-141 | 88.45 | 32.5 d | 145.4 (48.3%) |
| Ce-142 | Ce-143 | 11.11 | 33.03 h | 293.3 (42.8%) |

**Table 2** Past measurements of thermal neutron capture cross sections ($\sigma$) of $^{140,142}$Ce

| References | $^{140}$Ce $\sigma$ (b) | Reference | $^{142}$Ce $\sigma$ (b) |
| --- | --- | --- | --- |
| Katcoff [10] | 0.27±0.07 | Katcoff,1948 [10] | 0.95±0.18 |
| Pomerance [11] | 0.63 | Roy, 1948 [11] | 0.95±0.01 |
| Lantz [12] | 0.59±0.06 | Lyon, 1959 [17] | 0.91 |
| Alstad [13] | 0.54±0.04 | Alstad, 1967 [13] | 0.94±0.09 |
| Alian [18] | 0.68 | Torrel, 2012 [14] | 0.88±0.04 |
| Torrel [14] | 0.51±0.02 | | |
| Panikkath [15] | 0.44±0.02 | | |

hensive foundation for understanding the thermal neutron capture properties of cerium isotopes. The authors [10–17] of these measurements utilised natural cerium oxide (CeO$_2$) powder as the experimental material. The natural composition of $CeO_2$ includes a mix of cerium isotopes, predominantly $^{136,138,140,142}$Ce as shown in Table 1.
Most of the irradiation in these experiments were conducted using a reactor spectrum. Such a spectrum is essential for obtaining data that is relevant for reactor applications, as it reflects the actual operating environment of thermal nuclear reactors. Additionally, the measurement by Panikkath et al [15] was performed using a modified Americium-Beryllium (Am–Be) spectrum. The previous measurements are given in Table 2.

The investigation into the thermal neutron capture cross-section ($\sigma_{th}$) of cerium isotopes highlights a significant research gap due to the scarcity and inconsistency of available data. Despite cerium's crucial role in various nuclear applications, the lack of precise and comprehensive $\sigma_{th}$ measurements impedes its full potential. This issue is compounded by outdated data, primarily from before the 1970s, collected with low-resolution detectors and not-so-well-established data libraries, introducing considerable uncertainty. Additionally, the absence of covariance analysis [19] and detailed uncertainty reports in existing literature hinders the reliability and broader utilisation of the data. Furthermore, the unknown nature of neutron spectra at irradiation facilities emphasises the need for comprehensive investigations and neutron spectrum unfolding to optimise experimental conditions and improve result accuracy. This research gap impacts reactor design, nuclear fuel optimisation, and astrophysical studies, necessitating a harmonised and accurate dataset for cerium isotopes.

The present study aims to provide precise data of the thermal neutron capture cross-section for cerium isotopes, particularly $^{140}$Ce and $^{142}$Ce. Measurements are carried out using neutrons from an Am–Be source located inside a concrete bunker employing the Neutron activation method [20] and offline gamma spectrometry. These measurements are accompanied by a detailed uncertainty analysis. It includes a comprehensive covariance analysis [19] to investigate the inter-dependencies of different nuclear data quantities, as per the IAEA standards. Further, the neutron spectrum from the irradiation location was obtained by employing multiple foil activation technique and Monte Carlo simulations.

## 2 Experimental methods

### 2.1 Neutron activation and gamma-ray spectrometry

Natural cerium oxide (CeO$_2$) powder, with its isotopic abundances detailed in Table 1, served as the sample material for this study. A 1.8 g sample of natural CeO$_2$, comprising 1.66 g of pure cerium, was pelletised at the Materials Science Laboratory, Department of Physics, Manipal Institute of Technology (MIT), Manipal Academy of Higher Education (MAHE). The pelletisation was conducted under a pressure of 5 MPa, yielding a cylindrical pellet with dimensions of 4.3 mm in height and 6.5 mm in radius and a resultant density of 3.14 g/cm$^3$. It is noteworthy that the pelletisation process was performed without the addition of any binders, ensuring the purity of the sample.

To ensure the purity of the samples, irradiation was conducted immediately following the preparation process, effectively minimising any potential contamination risks.
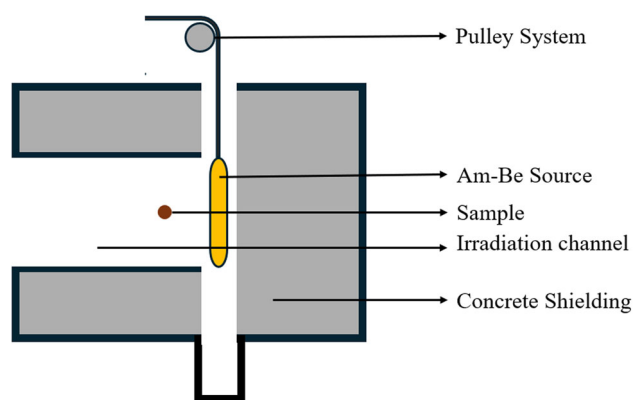
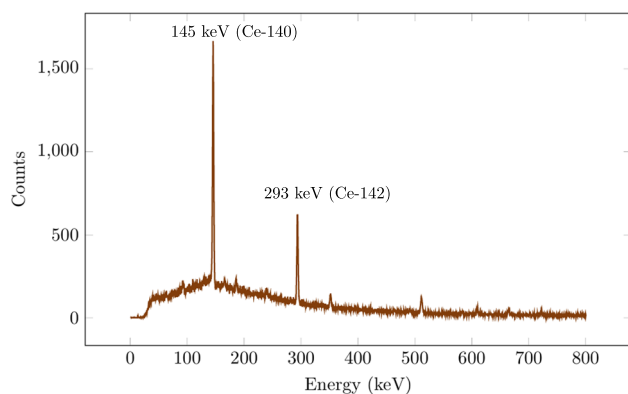**Fig. 1** Schematic diagram of the irradiation facility



**Fig. 2** Measured gamma-ray spectrum of $CeO_2$ sample

The sample was irradiated using a 16 Curie Americium-Beryllium (Am–Be) neutron source located at MIT, MAHE [21], for a continuous duration of 14.8 days. The Am–Be neutron source has a neutron yield of $4 \times 10^7$ neutrons per second in a $4\pi$ geometry. This source is enclosed within a concrete bunker that has an opening on one side to facilitate sample irradiation. The Am–Be neutron source is securely stored in an underground facility and is raised to the operational position using a pulley system, as depicted in Fig. 1 and 2. Due to multiple scattering within the concrete structure, the neutron spectrum from the Am–Be source undergoes moderation. For precise and consistent irradiation, the sample was positioned at a fixed distance of 8 cm from the neutron

source. This setup included a gold foil that functioned as a flux monitor to measure the neutron flux accurately.

The details regarding the experimental procedure, including spectroscopic data, are documented in Tables 3 and 4, and the spectrum of the irradiated cerium sample is shown in Fig. 3.

| Quantity | Ce-140 | Ce-142 | Flux monitor (Au-197) |
|---|---|---|---|
| Reaction | $(n, \gamma)$ | $(n, \gamma)$ | $(n, \gamma)$ |
| Half-life | 32.5 d | 33.03 h | 2.6 d |
| Gamma-lines Energy (keV) | 145.4 | 293.2 | 411.1 |
| Gamma-ray probability(%) | 48.3 | 42.8 | 95.6 |

## 2.2 Neutron spectrum unfolding

Neutron spectrum unfolding is crucial for accurately determining the distribution of neutron energies, which directly influences the material responses and experimental outcomes. Here the neutron source is enclosed within a concrete shielding material to ensure safety during experiments. The neutrons emitted from the Americium-Beryllium (Am–Be) source interact with the shielding materials, resulting in a modified neutron spectrum at the irradiation location. Consequently, determining the exact nature of the neutron spectrum at the irradiation location is crucial for conducting precise experiments. Various methods are available for unfolding the neutron spectrum [23–28]. Characterisation of neutron spectra, specifically from Beryllium-based neutron sources, has been extensively carried out using Monte Carlo simulations, followed by multi-foil activation techniques [29–34]. These methods combine computational modelling with experimental validation, providing a comprehensive understanding of the neutron spectra.

The present study employs a combination of experimental techniques and computational simulations to achieve this objective. In this case, we have employed the multi-foil activation technique to obtain experimental data and an iterative method to unfold the spectrum.
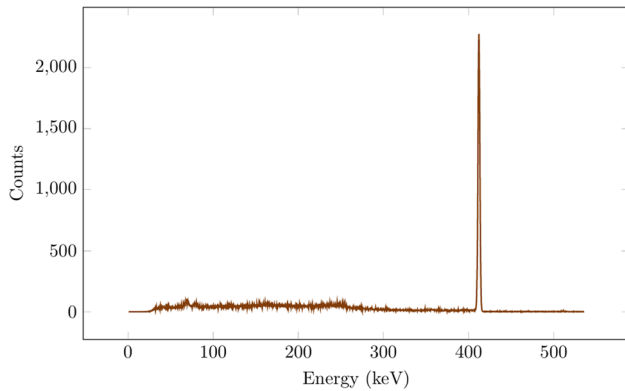
The unfolding process involves solving the Fredholm integral equation of the first kind, which is a well-established

**Table 3** Experimental details of cross-section measurements

| Quantity | Ce-140 | Ce-142 | Flux monitor (Au-197) |
|---|---|---|---|
| Mass (g) | 1.46 | 0.18 | 0.13 |
| Irradiation time (d) | 14.8 | 14.8 | 14.8 |
| Counting time (h) | 27 | 27 | 1 |
| Total counts | 11914 | 4798 | 11542 |

**Table 4** Experimental spectroscopic data used for cross-section measurements from NuDat3 [22]

| Isotopes | Gamma lines (KeV) | Intensity | Half lives | Efficiency | Sample mass | Irradiation time | Cooling time | Counting time | Counts |
|---|---|---|---|---|---|---|---|---|---|
| Ce-140 | 145 | 0.48 | 32.5 d | 0.10 | 1.66 | 1278,720 | 1380 | 97200 | 11,914 |
| Ce-142 | 293 | 0.42 | 33.03 h | 0.067 | 1.66 | 1278,720 | 1380 | 97200 | 4798 |
| Au-197 | 411 | 0.965 | 2.7 d | 0.050 | 0.13 | 1278,720 | 98,580 | 3600 | 20,248 |



**Fig. 3** Measured gamma-ray spectrum of Au flux monitor

mathematical approach in neutron spectrometry. Let $A$ represent the experimentally determined activities, $R$ denote the response matrix, and $\phi$ symbolise the unknown neutron spectrum. The equation can be expressed as [35]:
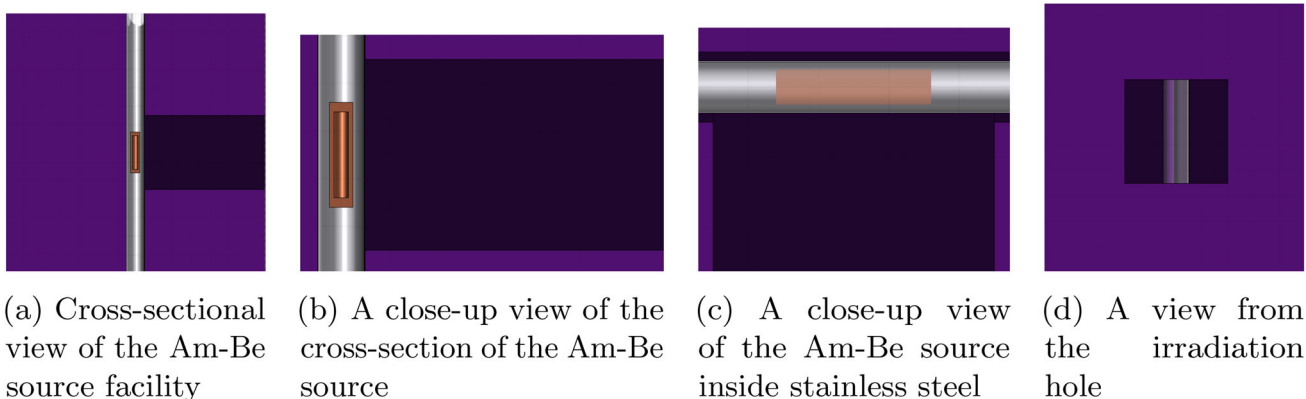
$$A = \int_E R(E)\phi(E)dE \tag{1}$$

For multiple foils, this equation is modified as follows:

$$A_i = \int_E \sigma_i(E)\phi(E)dE \tag{2}$$

where $\sigma$ is the cross-section and $i$ is the index of the foil. Different foils are irradiated under identical conditions.

We simulated neutron spectra at the irradiation location using Monte Carlo methods. The iterative nature of the unfolding method, where an initial guess of the spectrum is refined at each iteration to match the experimental data set, makes the resultant spectrum highly dependent on the initial input spectrum. We performed a detailed simulation of the source facility to provide an accurate initial estimate. The detailed simulation of the source facility using Monte Carlo N-Particle Transport Code (MCNP) provided valuable insights into the neutron transport and interactions within the shielding material. The simulation included the geometry of the doubly encapsulated Am–Be source, which consists of americium and beryllium encapsulated in stainless steel. The shielding materials were modelled accurately to reflect the actual experimental setup, including concrete and other materials used to attenuate and scatter the neutrons. The position of the samples in the irradiation facility was also precisely defined to replicate the experimental conditions. The simulation was executed using MCNP [36]. Figure 4 illustrates the geometry of the source setup. The output of the simulation, along with the bare Am–Be spectra, is depicted in Fig. 5. The simulation was carried out with $5 \times 10^7$ particle histories and using ENDF-VII[37]. The simulated spectrum has an uncertainty of 10–12%. From the figure, we can observe that the spectrum looks different, and the flux is maximum in the thermal region.

The multi-foil activation technique utilises various foils with different threshold reactions and capture cross-sections to characterize the neutron spectrum. In the present study, we



(a) Cross-sectional view of the Am-Be source facility

(b) A close-up view of the cross-section of the Am-Be source

(c) A close-up view of the Am-Be source inside stainless steel

(d) A view from the irradiation hole

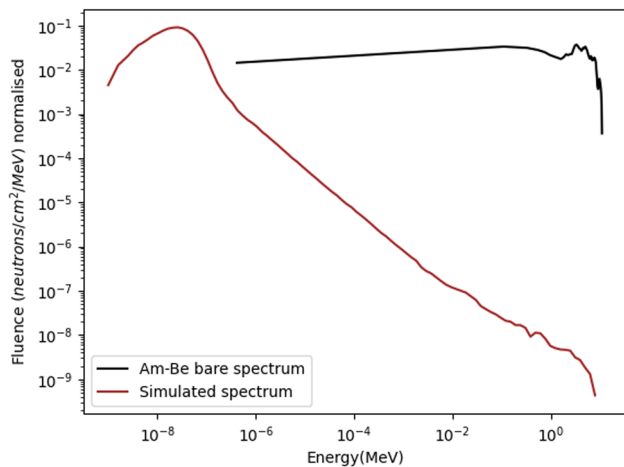**Fig. 4** Geometry of the Am–Be source facility

**Fig. 5** Comparision of the simulated spectra and the bare Am–Be spectra [38]

selected six different foils: $^{55}$Mn, $^{63}$Cu, $^{197}$Au, $^{58}$Ni, $^{115}$In, and $^{45}$Sc. Each foil has a well-known neutron capture cross-section that varies with neutron energy, allowing us to capture a broad spectrum of neutron energies. The detailed cross-section data for these foils are available, enabling precise calculation of neutron flux and energy spectrum.

The foils were irradiated at the exact location as the cerium samples using the Am–Be neutron source. All foils underwent irradiation under identical conditions to ensure consistency in the experimental setup. Post-irradiation, the activated foils were analysed using an HPGe detector. The gamma spectra of the activated foils were recorded, and the peaks corresponding to the specific gamma emissions of each isotope were identified with high precision. The photopeak areas were calculated to determine the activity of each foil. The activity measured from the multi-foil activation for all the foils is given in Table 5. These activities are directly related to the neutron flux and the cross-section of the reactions occurring in the foils, as described by Eq. 1.

The iterative unfolding method employed in this study involved adjusting the initial guess of the neutron spectrum based on the discrepancies between the simulated and experimental activities. This process was repeated until convergence was achieved, ensuring difference between the Estimated reaction rate and the measured reaction rate was less than 1%. Figure 6 shows the unfolded neutron spectrum of the Am–Be source at the irradiation location obtained from the SAND-II code [39].

### 2.3 Cross-section calculations and associated uncertainties

The efficiency ($\varepsilon$) of the HPGe detector was calculated using the Eq. 3.

$$\varepsilon = \frac{C}{A_0 I_\gamma e^{-\lambda t}} \tag{3}$$

Where $C$ is the photopeak counts, $A_0$ is the initial activity of the source at the time of manufacture, $I_\gamma$ is the branching ratio of the gamma line, $\lambda$ is the half-life, $t$ is the time elapsed until counting, $\Delta t$ is the time of counting. The efficiency variation of the detector as a function of energy is plotted in Fig. 7. The cross-section $\sigma$ of cerium was calculated using the formula given in [20], and it is shown in Eq. 4. $M$ is the mass number, $m$ is the mass of the sample, $\theta$ is the isotopic abundance, $\phi$ is the thermal neutron flux and $T_\lambda$ is the time factor. The sample was 4.3 mm thick and had a considerably large area, so corrections like self-shielding and geometric efficiency were carried out to get precise results. $F$ is the correction for self-shielding and $\epsilon$ is the geometric efficiency.

$$\sigma = \frac{FCM}{m\theta\phi\epsilon\varepsilon I_\gamma T_\lambda} \tag{4}$$

The time factor $T_\lambda$ is given in Eq 5. $t_i$ is the irradiation time, $t_d$ is the decay time, $t_c$ is the counting time.

$$T_\lambda = (1 - e^{-\lambda t_i})\frac{e^{-\lambda t_d}}{\lambda}(1 - e^{-\lambda t_c}) \tag{5}$$

The ratio of thermal to epithermal neutrons was determined to be 73.8% with the help of cadmium covers in our previous work [21]. We obtain the thermal neutron flux of $4.090 \times 10^3$ $n/cm^2$ at the irradiation location using standard gold foil, which was irradiated along with the cerium samples. This flux is used for the cross-section calculation. As we have a thick sample, we have performed the corrections for those as well. The correction due to the geometric efficiency $\epsilon$ can be done as shown in [40] as Eq 6. $d$ is the distance between the sample and the detector, and $r$ is the radius of the sample.

$$\epsilon = \frac{d^2}{r^2}ln\left(1 + \frac{r^2}{d^2}\right) \tag{6}$$

It is observed that cerium has a high attenuation coefficient for gamma rays, and the linear attenuation coefficient is heavily dependent on the density of the sample. The density of the pellet was measured to be 3.14 g/cc. The attenuation coefficients for different energies, along with correction, are given in a Table 6. The data was obtained from the NIST database [41]. The self-shielding $F$ of the sample is given in Eq 7. $\mu$ is the linear attenuation coefficient and $l$ is the thickness of the sample.

$$F = \frac{\mu l}{(1 - e^{-\mu l})} \tag{7}$$

**Table 5** Reaction rates of all the foils used for spectrum unfolding

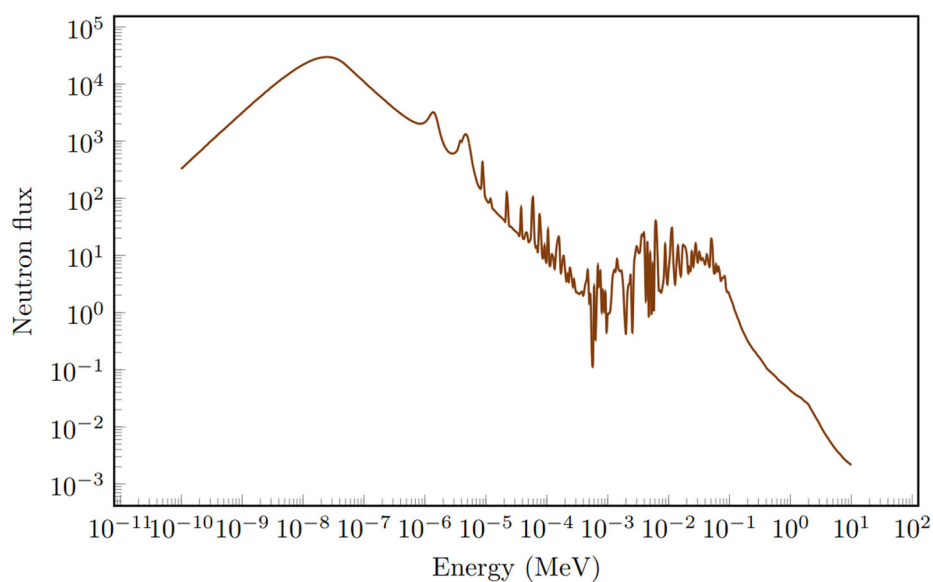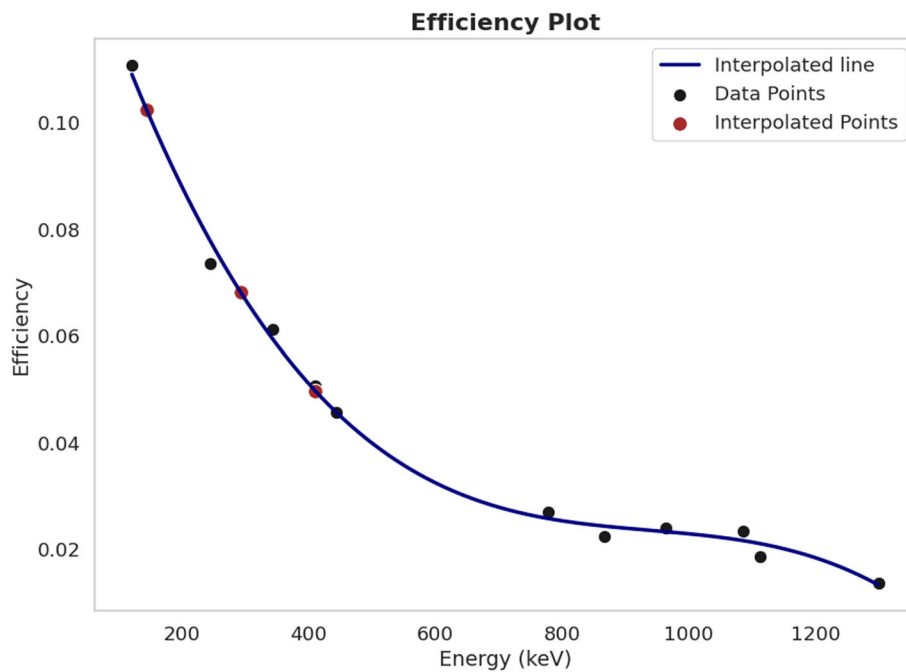| Foil | Induced reaction | Mass No | Mass of sample (g) | Half life (s) | Gamma energy (keV) | Abundance % | Reaction rate (/Atom/s) |
|------|------------------|---------|--------------------|---------------|--------------------|-------------|-------------------------|
| Mn | n,$\gamma$ | 55 | 0.043 | 9144 | 846 | 98.9 | 4.98E–20 |
| Sc | n,$\gamma$ | 45 | 0.048 | 7240,320 | 889 | 100 | 9.77E–20 |
| Au | n,$\gamma$ | 197 | 0.012 | 232,416 | 411 | 95.6 | 6.10E–18 |
| Cu | n,$\gamma$ | 63 | 0.005 | 45,720 | 511 | 37 | 3.55E–20 |
| In | n,$\gamma$ | 115 | 0.123 | 3240 | 1097 | 56 | 9.13E–18 |



**Fig. 6** Unfolded neutron spectrum of the Am–Be source at the irradiation location from SAND-II



**Fig. 7** Absolute efficiency curve of the HPGe detector

**Table 6** Correction factors for the calculation of cross-section of Cerium samples

| Ce Isotopes | Geometric efficiency $\epsilon$ | Linear attenuation Coefficient $\mu$ (/cm) | Self-shielding factor $f_s$ |
|---|---|---|---|
| 140 | 9.60E–01 | 1.69 | 1.40 |
| 142 | 9.60E–01 | 0.6 | 1.10 |

## 2.4 Covariance analysis

The covariance (correlation) analysis is a mathematical tool that calculates the best estimate of the uncertainty as well as cross correlations between measured quantities. The covariance quantifies the degree to which two variables change together. Mathematically, it can be written as [19]:

$$Cov(x, y) = \frac{\sum(x_i - \bar{x})(y_i - \bar{y})}{N} \tag{8}$$

$$Cor(x, y) = \frac{Cov(x, y)}{\Delta x \, \Delta y} \tag{9}$$

The measured cross-section is correlated with the monitor reaction and with the detector efficiencies at all six energies. The uncertainty in the detector efficiencies has been calculated first, and then estimated the cross-section correlations using these values [42]. Detector efficiency is the function of four parameters, $\varepsilon = f(C, I_\gamma, A_0, T_{\frac{1}{2}})$. We can use the quadratic sum formula to compute the uncertainties in the efficiency given by

$$\left(\frac{\Delta \varepsilon_i}{\varepsilon_i}\right)^2 = \left(\frac{\Delta C_i}{C_i}\right)^2 + \left(\frac{\Delta I_{\gamma_i}}{I_{\gamma_i}}\right)^2$$
$$+ \left(T \ln 2 \frac{\Delta t_{1/2}}{t_{1/2}^2}\right)^2 + \left(\frac{\Delta A_0}{A_0}\right)^2 \tag{10}$$

The partial uncertainties in the efficiencies related to four different attributes are illustrated in Table 7. The covariance matrix for the detector efficiencies can be expressed as follows:

$$(V_\epsilon)_{ij} = \sum_r e_{ir} S_{ijr} e_{jr} \tag{11}$$

Here, $e_{ir}$ and $e_{jr}$ are diagonal matrices, and $S_{ijr}$ represent the micro-correlation matrices. In cases where elements are uncorrelated, $S_{ijr}$ can be represented by an $(n \times n)$ identity matrix. For cases of complete correlation, $S_{ijr}$ is an $(n \times n)$ matrix with all elements set to "1." For partial correlations, $S_{ijr}$ can be an $(n \times n)$ matrix with elements where $0 < S_{ijr} < 1$. The micro-correlation matrices for the attributes

$(C, I_\gamma, A_0, t_{1/2})$ can be represented as:

$$\begin{bmatrix} 1 & 0 & 0 \\ 0 & 1 & 0 \\ 0 & 0 & 1 \end{bmatrix}, \begin{bmatrix} 1 & 0 & 0 \\ 0 & 1 & 0 \\ 0 & 0 & 1 \end{bmatrix}, \begin{bmatrix} 1 & 1 & 1 \\ 1 & 1 & 1 \\ 1 & 1 & 1 \end{bmatrix}, \begin{bmatrix} 1 & 1 & 1 \\ 1 & 1 & 1 \\ 1 & 1 & 1 \end{bmatrix}$$

The covariance matrix created from Eqs. 10 and 11 is shown in Table 8.

The relationship between the efficiencies, $\epsilon_i$, used in the cross-section calculations can be expressed as:

$$\ln \epsilon_i = \sum_m p_m (\ln E_i)^{m-1} \tag{12}$$

where $\epsilon_i$ are the efficiencies, $p_m$ are the fitting parameters of order $m$, and $E_i$ are the corresponding $\gamma$-ray energies. Using the linear model $Z = AP$, the solution to Eq. 12 can be determined. Here, the column matrix $Z$ is defined by $z_i = \ln \epsilon_i$, $A$ is a design matrix with elements $A_{il} = (\ln E_i)^{l-1}$, and $P$ is the matrix with elements $p_m$. The elements of matrix $P$ are obtained using the least squares method. The solution parameters are derived using the covariance matrix $V_p = (A'V_z^{-1}A)^{-1}$ as shown in Eq. 13:

$$\hat{P} = \hat{V}_P(A'V_z^{-1}Z) \tag{13}$$

where the matrix $V_z$ is obtained using the following Eq. 14:

$$(V_z)_{ij} = \frac{(V_\epsilon)_{ij}}{\langle \epsilon_i \rangle \langle \epsilon_j \rangle} \tag{14}$$

In the final step, the goodness of fit is calculated using Eq. 15:

$$\chi_m^2 = (Z - AP)'V_z^{-1}(Z - AP) \tag{15}$$

The chi square fitting has a value of 0.716061353. The fitting parameters in the fitting sequence are: $-3.755735986$, $-0.844304651$, $-0.991910551$, $-1.162012194$, $-0.340517991$. The final correlation matrix for the measured efficiencies of the sample and monitor reaction is shown in Table 9.

The ratio measurement technique [19] was applied in the covariance analysis, as the sample reaction cross-sections $\langle \sigma_r \rangle$ were normalised relative to the monitor reaction cross-sections $\langle \sigma_m \rangle$. The current reaction parameters are denoted

**Table 7** Partial uncertainties in the efficiency of detector measured from $^{152}$Eu point source

| Gamma line | Partial uncertainty due to attributes | | | | Total uncertainty |
|---|---|---|---|---|---|
| keV | $C$ ($r = 1$) $\times 10^{-3}$ | $I_\gamma$ ($r=2$) $\times 10^{-4}$ | $A_0$ ($r = 3$) $\times 10^{-4}$ | $T_{1/2}$($r=4$) $\times 10^{-6}$ | $\times 10^{-2}$ |
| 121.7817 | 0.981205 | 6.08357 | 14.8461 | 5.71534 | 0.18807 |
| 244.6974 | 1.64790 | 3.81965 | 9.86692 | 3.79850 | 0.19583 |
| 411.1165 | 2.78089 | 2.46451 | 5.80396 | 2.23437 | 0.28515 |
| 778.9045 | 0.817899 | 1.68335 | 3.72353 | 1.43346 | 0.09143 |
| 964.057 | 0.728837 | 1.17789 | 3.34154 | 1.28640 | 0.08104 |
| 1299.142 | 1.90473 | 0.70640 | 2.24183 | 0.863044 | 0.19192 |

**Table 8** Covariance matrix for detector efficiencies

| | | | | | |
|---|---|---|---|---|---|
| $3.53696 \times 10^{-6}$ | | | | | |
| $1.46487 \times 10^{-6}$ | $3.83506 \times 10^{-6}$ | | | | |
| $8.61674 \times 10^{-7}$ | $5.72681 \times 10^{-7}$ | $8.13092 \times 10^{-6}$ | | | |
| $5.52807 \times 10^{-7}$ | $3.67403 \times 10^{-7}$ | $2.16115 \times 10^{-7}$ | $8.35943 \times 10^{-7}$ | | |
| $4.96096 \times 10^{-7}$ | $3.29712 \times 10^{-7}$ | $1.93945 \times 10^{-7}$ | $1.24425 \times 10^{-7}$ | $6.56739 \times 10^{-7}$ | |
| $3.32829 \times 10^{-7}$ | $2.21203 \times 10^{-7}$ | $1.30117 \times 10^{-7}$ | $8.34765 \times 10^{-8}$ | $7.49129 \times 10^{-8}$ | $3.68324 \times 10^{-6}$ |

**Table 9** The uncertainty in the detector efficiency and the correlation matrix for the sample and the monitor

| Gamma-energy (keV) | Uncertainty | Covariance matrix | | | Correlation matrix | | |
|---|---|---|---|---|---|---|---|
| 145.4 | 0.00724 | $5.24527 \times 10^{-5}$ | | | 1 | | |
| 293.2 | 0.00391 | $-1.54663 \times 10^{-5}$ | $1.53202 \times 10^{-5}$ | | $-0.54560$ | 1 | |
| 411.1 | 0.00302 | $-1.75736 \times 10^{-5}$ | $1.08533 \times 10^{-5}$ | $9.14132 \times 10^{-6}$ | $-0.80255$ | 0.91712 | 1 |

by the subscript 'r', while the monitor reaction parameters are denoted by the subscript "m".

$$\langle \sigma_r \rangle = \langle \sigma_m \rangle \frac{C_r I_{\gamma m} \epsilon_m T_{\lambda m}}{C_m I_{\gamma r} \epsilon_r T_{\lambda r}} \tag{16}$$

with the time factor $T_\lambda$ defined as:

$$T_\lambda = \frac{(1 - e^{-\lambda t_i})(1 - e^{-\lambda t_d})(e^{-\lambda t_c})}{\lambda} \tag{17}$$

The uncertainty related to each attribute in Eq. 16 can be determined using the quadratic sum formula. The attribute $f$ has five sources of uncertainty: $t_i$, $t_c$, $t_w$, $\lambda_r$, and $\lambda_m$ among all the attributes in Eq. 16. The uncertainty in the last two terms (decay constants) is related to the cross-section through the exponential function. Consequently, the uncertainty in the decay constants in terms of time factors is defined as follows:

$$\left( \frac{\Delta f}{f} \right)^2 = s_{f\lambda}^2 \left( \frac{\Delta \lambda}{\lambda} \right)^2 \tag{18}$$

The uncertainty in the decay constant is related to the term $\Delta T_{1/2}$ through the relation $\Delta \lambda = \frac{\ln 2 \, \Delta T_{1/2}}{T_{1/2}^2}$. Thus, the relative sensitivity can be defined as:

$$s_{f\lambda} = \left( \frac{\lambda t_i e^{-\lambda t_i}}{1 - e^{-\lambda t_i}} - \lambda t_d + \frac{\lambda t_c e^{-\lambda t_c}}{1 - e^{-\lambda t_c}} - 1 \right) \tag{19}$$

The uncertainties associated with different parameters are shown in Table 10. The final correlation matrix for the measured reaction cross-section is shown in Table 11.

## 3 Result and discussions

In the present study, we measured the thermal neutron capture cross-sections ($\sigma_{th}$) for cerium isotopes, specifically cerium-140 and cerium-142, using natural cerium oxide (CeO$_2$) samples irradiated with an Americium-Beryllium (Am–Be) neutron source. This marks the first time that the thermal neutron capture cross-section for cerium-142 has been measured using an Am–Be neutron source. The measurements were conducted using standard neutron activation analysis,

**Table 10** Uncertainties associated with the cross-section calculations for sample and monitor

| Reaction | Counts | Efficiency | $I_\gamma$ | Time factor ($T_\lambda$) | Mass (m) | Atomic mass | Cross-section |
|---|---|---|---|---|---|---|---|
| $^{140}Ce(n,\gamma)^{141}Ce$ | 0.010072 | 0.058848 | 0.0014534 | 0.000427 | 0.000742745 | 8.57722E–11 | – |
| $^{142}Ce(n,\gamma)^{143}Ce$ | 0.010004 | 0.055858 | 0.0029322 | 0.000194 | 0.000742745 | 8.39694E–11 | – |
| $^{197}Au(n,\gamma)^{198}Au$ | 0.007215 | 0.074064 | 0.0041173 | 0.000796 | 0.016666667 | 2.26804E–02 | 6.0924E–10 |

**Table 11** Correlation matrix for the measured reaction cross-sections

| Reaction | Gamma line (keV) | Covariance matrix | | Correlation matrix | |
|---|---|---|---|---|---|
| $^{140}Ce(n,\gamma)^{141}Ce$ | 145 | 0.0099095 | | 1 | |
| $^{142}Ce(n,\gamma)^{143}Ce$ | 293 | 0.0062953 | 0.0095718 | 0.646389 | 1 |

**Table 12** Measured cross-section compared with previous measurements from Table 2 and evaluated data libraries

| Reaction | Cross-section(b) | Range of previous measurements (b)[9] | Evaluated data libraries ENDF [43] | JEFF [44] | JENDL [2] |
|---|---|---|---|---|---|
| $^{140}Ce(n,\gamma)^{141}Ce$ | $0.54 \pm 0.03$ | 0.27–0.68 | 0.57752 | 0.57461 | 0.570395 |
| $^{142}Ce(n,\gamma)^{142}Ce$ | $0.83 \pm 0.04$ | 0.88–0.95 | 0.96504 | 0.96504 | 0.961195 |

and the gamma emissions from the irradiated samples were analyzed using an HPGe detector. The neutron spectrum at the irradiation site was precisely determined through neutron spectrum unfolding using Monte Carlo simulations and multi-foil activation techniques. The unfolded spectrum is plotted in Fig. 6. The thermal neutron capture cross-section for cerium-140 was found to be $0.54 \pm 0.03$ barns, and for cerium-142, it was $0.83 \pm 0.04$ barns as shown in Table 12. These values align closely with previously reported measurements, which report cross-sections for cerium-140 ranging from 0.44 to 0.68 barns, and for cerium-142, from 0.88 to 0.95 barns. The measured cross sections are compared with previous measurements along with the evaluated libraries [2,43,44] in Figs. 8 and 9. It can be seen from the Figs. 6 and 7 that the presently measured thermal cross-section values of $^{140}$Ce and $^{142}$Ce is lower than the evaluated data but having higher accuracy compared to the previous measurements with larger uncertainties. Further, we performed a detailed covariance analysis, marking the first time such an analysis has been conducted for these measurements, to quantify the uncertainties and inter-dependencies in our measurements. The detailed uncertainty and covariance analysis performed in the present study provides a deeper understanding of the precision of our measurements and highlights the critical factors influencing the accuracy of $\sigma_{th}$ values. This approach enhanced the understanding of the reliability and limitations of the experimental measurements, providing a robust dataset for nuclear data libraries. Further, at low incident neutron energies the nuclear reaction cross section exhibits a distinct resonance structure. Generally, R-matrix theory is applied, which provides a sufficiently accurate but phenomenological description of the resonance region. We see the R-matrix formalism as relevant for future discussions or applications of our research.

## 4 Conclusion

The present study provides precise measurements of the thermal neutron capture cross-sections ($\sigma_{th}$) for cerium isotopes, specifically $^{140}$Ce and $^{142}$Ce, using natural cerium oxide ($CeO_2$) and an Americium-Beryllium (Am–Be) neutron source. The neutron spectrum from the irradiation location was obtained by employing multiple foil activation technique and spectrum unfolding method. The refined neutron spectrum from the Am–Be source improved our understanding of neutron interactions in the mixed-field environments. The results, $0.54 \pm 0.03$ barns for $^{140}$Ce and $0.83 \pm 0.04$ barns for cerium-142, align well with previous data. Comprehensive covariance and uncertainty analyses are also performed for the first time for the cerium isotopes. It is found that the presently measured thermal cross-section values of $^{140}$Ce and $^{142}$Ce is lower than the evaluated data but having higher accuracy compared to the previous measurements with larger uncertainties. Thus, the current state of nuclear data evaluation requires improvement for cerium isotopes.

**Fig. 8** Experimentally measured $^{140}$Ce(n,$\gamma$)$^{141}$Ce reaction cross-section compared with the literature data and evaluated libraries



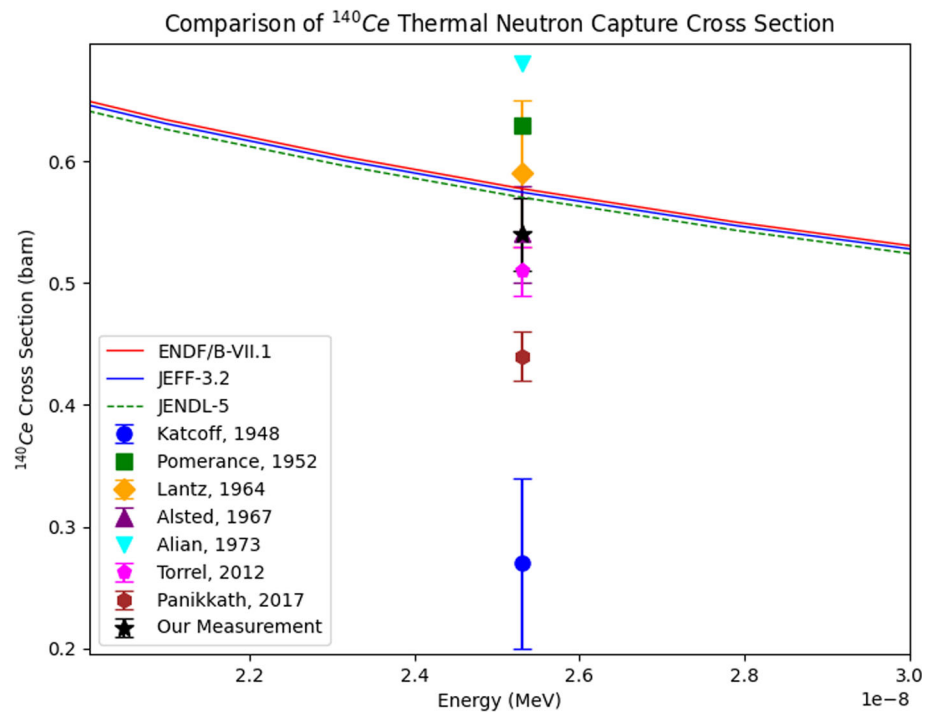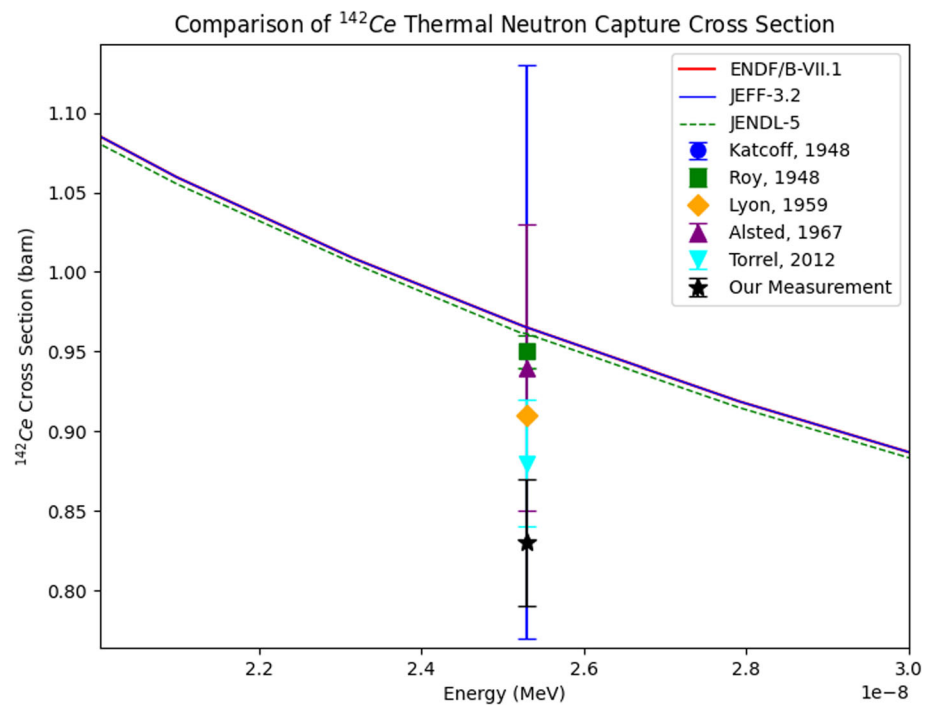**Fig. 9** Experimentally measured $^{142}$Ce(n,$\gamma$)$^{143}$Ce reaction cross-section compared with the literature data and evaluated libraries

**Data Availability Statement** My manuscript has associated data. [Author's comment: All data generated or analysed during this study are included in this published article.]

**Code Availability Statement** My manuscript has no associated code/software. [Author's comment: Code/Software sharing not applicable to this article as no code/software was generated or analysed during the current study.]

# References

1. D. R. Lide, CRC handbook of chemistry and physics. Vol. 85. CRC press (2004)
2. K. Shibata et al., JENDL-4.0: a new library for nuclear science and engineering. J. Nucl. Sci. Technol. **48**(1), 1–30 (2011)
3. M. Herman et al., Status of ENDF/B-VII. 1 Library. In: NEA/NSC/WPEC/DOC, p. 431 (2011)
4. Said F, Mughabghab, Atlas of neutron resonances: resonance parameters and thermal cross sections. Z= 1-100. Elsevier (2006)
5. F. Kappeler et al., Neutron capture cross sections of the cerium isotopes for s- and p-process studies. Phys. Rev. C **53**, 1397–1408 (1996). https://doi.org/10.1103/PhysRevC.53.1397
6. R.N. Sahoo et al., Stellar s-process neutron capture cross section of Ce isotopes. Phys. Rev. C **109**(2), 025808 (2024)
7. S. Amaducci et al., Measurement of the Ce 140 (n, $\gamma$) Cross Section at n_TOF and Its Astrophysical Implications for the Chemical Evolution of the Universe. Phys. Rev. Lett. **132**(12), 122701 (2024)
8. F.G. Kondev et al., The NUBASE2020 evaluation of nuclear physics properties. Chin. Phys. C **45**(3), 030001 (2021)
9. V.V. Zerkin, B. Pritychenko, The experimental nuclear reaction data (EXFOR): extended computer database and Web retrieval system. Nucl. Instrum. Methods Phys. Res. Sect. A **888**, 31–43 (2018)
10. S. Katcoff et al., Neutron absorption cross sections of radioactive La140 and two stable cerium isotopes. J. Chem. Phys. **17**(4), 421–424 (1949)
11. H. Pomerance, Thermal neutron capture cross sections. Phys. Rev. **88**(2), 412 (1952)
12. P.M. Lantz, C.R. Baldock, L.E. Idom, Thermal-neutron capture cross section and resonance capture integral of Ce140 and effective capture cross section of Ce141. Nucl. Sci. Eng. **20**(3), 302–306 (1964)
13. J. Alstad, T. Jahnsen, A.C. Pappas, Thermal neutron capture cross section and resonance capture integral of the lanthanide nuclei 14Ce, 142Ce, 146Nd, 158Nd, 150Nd and 159Tb. J. Inorg. Nucl. Chem. **29**(9), 2155–2160 (1967)
14. S. Torrel, K.S. Krane, Neutron capture cross sections of 136, 138, 140, 142 Ce and the decays of 137 Ce. Phys. Rev. C **86**(3), 034340 (2012)
15. P. Panikkath, P. Mohanakrishnan, Thermal neutron capture cross-section and resonance integral measurements of 139La (n, $\gamma$) 140La and 140Ce (n, $\gamma$) 141Ce using a Am-Be neutron source. Eur. Phys. J. A. **53**(3), 46 (2017)
16. L.P. Roy, L. Yaffe, Thermal neutron capture cross section of Ce142. Can. J. Chem. **34**(8), 1023–1026 (1956)
17. W.S. Lyon, Reactor neutron activation cross sections for a number of elements. Nucl. Sci. Eng. **8**(5), 378–380 (1960)
18. A. Alian, H. Born, J. Kim, Thermal and epithermal neutron activation analysis using the monostandard method. J. Radioanal. Nucl. Chem. **15**(2), 535–546 (1973)
19. N. Otuka et al., Uncertainty propagation in activation cross section measurements. Radiat. Phys. Chem. **140**, 502–510 (2017)
20. R.R. Greenberg, P. Bode, E.A. De Nadai Fernandes, "Neutron activation analysis: a primary method of measurement. Spectrochim. Acta Part B **66**(3–4), 193–241 (2011)
21. Guruprasad et al., Measurement of flux distribution of an AmBe neutron source and estimation of two group integral capture cross-sections. Nucl. Part. Phys. Proc. **341**, 53–55 (2023)
22. "NuDat," Brookhaven National Labortory. www.nndc.bnl.gov/nudat3/
23. F.D. Brooks, A scintillation counter with neutron and gamma-ray discriminators. Nucl. Inst. Methods **4**(3), 151–163 (1959)
24. I. Murata et al., Neutron and gamma-ray source-term characterization of AmBe sources in Osaka University. Prog. Nucl. Sci. Technol. **4**, 345–348 (2014)
25. R.L. Bramblett, R.I. Ewing, T.W. Bonner, A new type of neutron spectrometer. Nucl. Inst. Methods **9**(1), 1–12 (1960)
26. M. Matzke, K. Weise, Neutron spectrum unfolding by the Monte Carlo method. Nucl. Instrum. Methods Phys. Res. Sect. A **234**(2), 324–330 (1985)
27. S. Itoh, Neutron spectra unfolding with maximum entropy and maximum likelihood. J. Nucl. Sci. Technol. **26**(9), 833–843 (1989)
28. V. Suman, P.K. Sarkar, Neutron spectrum unfolding using genetic algorithm in a Monte Carlo simulation. Nucl. Instrum. Methods Phys. Res. Sect. A **737**, 76–86 (2014)
29. P. Buffa, S. Rizzo, E. Tomarchio, A monte carlo-aided design of a modular 241Am-Be neutron irradiator. Nucl. Technol. Radiat. Protect. **28**(3), 265–272 (2013)
30. Z. Vykydal, M. Králik, Characterisation of the graphite moderated thermal neutron field at CMI. Radiat. Prot. Dosim. **180**(1–4), 51–55 (2018)
31. L.E. Cevallos-Robalino et al., Monte Carlo design and experimental characterization of a moderator device to produce a thermal neutron source from a 241Am/9Be source. Radiat. Phys. Chem. **168**, 108599 (2020)
32. M. Stefanik et al., Neutron field measurement of p (35)+ Be source using the multi-foil activation method. Radiat. Prot. Dosimetry. **180**(1–4), 377–381 (2018)
33. A.H. Willey, T.A. DeVol, N.E. Martinez, Thermal neutron characterization and dose modeling of a 239PuBe alpha-neutron source. Health Phys. **117**(6), 669–679 (2019)
34. N. Marchese et al., Neutron and gamma-ray radiation fields characterisation in a 241Am-Be irradiator in view of its use as research testing tool. Radiat. Phys. Chem. **170**, 108705 (2020)
35. E.M. Zsolnay, E.J. Szondi, Neutron spectrum determination by multiple foil activation method. Periodica Polytechnica Electr. Eng. (Arch.) **26**(1–2), 31–46 (1982)
36. J.F. Briesmeister, MCNP-A general Monte Carlo code for neutron and photon transport'. In: LA-7396-M (1986)
37. J. L. Conlin et al., MENDF71x. Multigroup neutron cross section data tables based upon ENDF/B-VII. 1. In: Tech. rep. Los Alamos National Lab.(LANL), Los Alamos, NM (US) (2015)
38. Anonymus AC03347667, Compendium of neutron spectra and detector responses for radiation protection purposes. Internat. Atomic Energy Agency (2001)
39. S. Berg, W.N. McElroy, A computer-automated iterative method for neutron flux spectra determination by foil activation, volume II. Sand II (spectrum analysis by neutron detectors II) and associated codes. Technical Report, April 1966–July 1967. Tech. rep. Atomics International, Canoga Park, Calif. (1967)

40. A.K. Chakraborty et al., Efficiency calibration of $\gamma$-ray detector for extended sources. Pramana **92**(4), 67 (2019)

41. NIST Public Access Plan. "National Institute of Standards and Technology (NIST)"

42. A. Hingu et al., Cross-sections for production of In115m by quasi-monoenergetic neutrons within 7–20 MeV. Radiat. Phys. Chem. **199**, 110270 (2022)

43. D.A. Brown et al., ENDF/B-VIII. 0: the 8th major release of the nuclear reaction data library with CIELO-project cross sections, new standards and thermal scattering data. Nucl. Data Sheets **148**, 1–142 (2018)

44. O. Cabellos, Processing and validation of JEFF-3.1. 2 cross-section library into various formats: ACE, PENDF, GENDF, MATXSR and BOXER. Nucl. Data Sheets **118**, 456–458 (2014)